



## Nano-structured platinum group metal-free catalysts and their integration in fuel cell electrode architectures



Alexey Serov<sup>a</sup>, Andrew D. Shum<sup>b</sup>, Xianghui Xiao<sup>c</sup>, Vincent De Andrade<sup>c</sup>, Kateryna Artyushkova<sup>a</sup>, Iryna V. Zenyuk<sup>b,\*</sup>, Plamen Atanassov<sup>a,\*</sup>

<sup>a</sup> Department of Chemical & Biological Engineering, Center for Micro-Engineered Materials, University of New Mexico, Albuquerque, NM 87131, USA

<sup>b</sup> Department of Mechanical Engineering, Tufts University, 200 College Avenue, Medford, MA 02155, USA, USA

<sup>c</sup> Advanced Photon Source, Argonne National Laboratory, Argonne, IL 60439, USA

### ARTICLE INFO

**Keywords:**

Fuel-cells  
Platinum group metal-free catalysts  
X-ray computed tomography  
Water management

### ABSTRACT

The novel platinum group metal-free (PGM-free) catalyst for the oxygen reduction reaction (ORR) is synthesized by a modified sacrificial support method (SSM). The catalyst chemical/surface composition is studied by X-ray photoelectron spectroscopy, and the morphology of the material is observed using both HR-SEM and HR-TEM, demonstrating the open-frame, self-supported catalysts. This new catalyst's electrochemical performance is evaluated by polarization curves and has behaviour comparable to the state-of-the-art PGM-free catalysts. Meso-structure imaging shows pores on the order of 100 nm, the mean size of the individual silica particles in the sacrificial support. For the first time, PGM-free catalyst layer (CL) morphology in a membrane electrode assembly (MEA) is studied in detail by combined nano- and micro X-ray computed tomography (CT) and interpretational modelling. The highly inhomogeneous, high-tortuosity, through-thickness structure of the CL is observed with micro-CT. The nano-CT method for these thick PGM-free electrodes is not sufficient to capture the full through-thickness morphology of these electrodes. Water retention curves suggest water pooling at the MEA components' interfaces and significant dependence of capillary pressure and saturation on through-thickness location. This study is the first of its kind to identify morphology-dependent transport losses in the thick PGM-free electrodes using scale-bridging between meso-, micro-, and macro.

### 1. Introduction

Last decade was marked with the startling introduction of fuel cell technology as one of the mainstream automotive development directions towards zero-emission vehicles (ZEV). The introduction of fuel cell vehicles (FCV) for demonstration and fleet lease was dramatically shifted towards the marketplace with the launch of the Toyota Mirai, the first commercially available FCV [1]. However, at the moment, the price of the FCV (57,500 USD) does not allow this ZEV to compete with conventional internal combustion engine (ICE) automobiles in the corresponding category and market niche. The high price of the Toyota Mirai stems from a combination of many factors, one of the most important being the fuel cell stack cost. Manufacturing and materials costs are substantial components of the stack cost, the catalysts and the MEA remaining the most important contributors. According to DOE Hydrogen Program FY 2010 Annual Progress Report, the price of platinum catalysts can be up to 40% of the whole fuel cell stack cost [2].

Attempts to substitute expensive platinum with other platinum

group metals (PGMs) were previously reported. The most active non-platinum materials for the oxygen reduction reaction (ORR) were found to be RuSe<sub>x</sub> and Pd-based catalysts [3–7]. However, the intrinsic stabilities of the electrocatalysts were not sufficient for long term operation of the catalysts as cathodes in proton exchange membrane fuel cells (PEMFCs) [8]. It should also be noted that the prices of platinum group metals, such as Ru, Pd, and Ir, are currently lower than that of Pt because of limited use (low demand), not high supply. All PGMs are extremely rare on the Earth's surface, and their sources are concentrated in very few sites globally. Their mining is exceptionally environmentally hazardous and a source of labour and political turmoil. The regional over-concentration of PGMs, their scarcity, and volatility of their price all present serious socio-economic and market factors that could potentially limit the wide spread of fuel cell technology through automotive applications (FCV), stationary heat-and-power generation, distributed/backup power, portable power, energy storage with regenerative fuel cells, and hydrogen production by electrolysis. Earth abundant catalysts present an alternative to PGMs as they provide a

\* Corresponding authors.

E-mail addresses: [Iryna.Zenyuk@tufts.edu](mailto:Iryna.Zenyuk@tufts.edu) (I.V. Zenyuk), [plamen@unm.edu](mailto:plamen@unm.edu) (P. Atanassov).

base for materials-unlimited energy technology, thus building a path towards sustainable environmentally benign deployment of a hydrogen economy.

At the moment, one of the most promising paths to FC stack cost reduction is the substitution of platinum catalysts for platinum group metal-free (PGM-free) electrocatalysts. The most advanced class of such materials is transition metal (iron)-nitrogen-carbon (Fe-N-C) catalysts for the electro-reduction of oxygen on the cathode side of the membrane electrode assembly (MEA) [9–21]. Substantial progress in these catalysts' development towards increasing ORR activity has been achieved over the last decade with the main evaluation criteria being the voltammetric study of the reduction of oxygen dissolved in the liquid electrolyte by the Rotating Disk Electrode (RDE) technique. However, to bring the development of Fe-N-C catalysts to the new competitive level of conventional PGM materials, the evolution and validation paradigm should be shifted to the integration of PGM-free catalysts into the catalytic layer. This presents a new set of challenges as the Fe-N-C catalysts are mainly carbon based [14–17] with low bulk density (high porosity) and presumed low density of ORR active sites. As a result, current stage PGM-free CLs are usually much thicker than the ones based on PGM catalysts.

At the moment, the solution to achieve reasonable activity is increasing the loading of catalyst to the 3–4 mg cm<sup>−2</sup> level. Compared to conventional PGM electrodes, PGM-free electrodes, due to these high catalyst loadings, are about an order of magnitude thicker, depending on preparation method (5 μm for PGM vs. 50–100 μm for PGM-free). The state-of-the-art power densities achieved for Fe-N-C catalysts are up to 1 W cm<sup>−2</sup> [22–24]. The increased thickness of these electrodes presents a challenge for the design of CL morphology that accommodates all the relevant transport properties. Oxygen, protons, and electrons have to traverse longer distances, resulting in increased mass-transport overpotential and Ohmic losses [25,26]. A recent study has shown that mass-transport loss at a current density of 1 A cm<sup>−2</sup> can be as large as 100 mV; [27] however, limited insight was given into the electrode structure causing this performance limitation. Shui et al. have shown that rational design of the CL with sufficient amount of pores larger than 50 nm by using nanofibrous structures to enhance mass transport resulted in high peak power density of 0.9 W cm<sup>−2</sup> (compared to 0.3 W cm<sup>−2</sup> for conventional design) [22]. Starinha et al. compared three PGM-free CLs with varied morphologies and concluded that higher pore connectivity translated into higher current densities, whereas higher porosity and roughness did not [14]. From a water management perspective, little is known about the local wettability of the PGM-free electrodes. A modelling study identified that key properties for the CL development are increased hydrophobicity (lower liquid water saturation) and lower ionomer tortuosity (higher conductivity) [28]. Optimizing electrode structure to accommodate all the transport processes is a key challenge and requires a detailed understanding of morphological features on the nano- and micro-scales.

Previously, the morphological structure of PGM-free electrodes was characterized with FIB-SEM [14] and nano-X-ray computed tomography (CT) [29], and the water distribution within these electrodes was studied with neutron radiography [30]. The first two methods are able to resolve nano-scale features of mesopores and smaller macropores (< 1 μm) within the catalyst support; however, due to a limited field-of-view (FOV), these techniques cannot resolve larger macropores (> 1 μm) within the representative elementary volume (REV). Neutron radiography is limited to a resolution of ~10 μm [31], the same order of magnitude as the larger macropores and agglomerates within this electrode.

Micro X-ray CT, with a spatial resolution of ~1 μm and FOV of 3.2–4 mm, fits between the length-scales of FIB-SEM and nano-X-ray CT on one end and neutron radiography on the other and is well-suited to characterize the larger macropores and agglomerate structures of the PGM-free electrode. Previously, micro X-ray CT has been extensively used to report properties of PEMFC gas-diffusion layers (GDLs) [32,33].

To the best of the authors' knowledge, this is the first article to report micro-X-ray CT imaging data for PGM-free electrodes. Furthermore, this study presents an attempt to bridge the scales between nano- and micro.

In this article, we present a comprehensive framework to understand the coupling between material chemistry and morphology on various length-scales for PGM-free catalysts. In this framework, the PGM-free catalyst is subjected to rigorous characterization as explained next. The state-of-the-art PGM-free catalyst was synthesized, and its surface chemistry was analyzed with XPS. The overall performance within a fuel cell was evaluated by fabricating a GDE and measuring a polarization curve. Furthermore, the catalyst and CL morphology were studied with SEM, TEM, and nano- and micro X-ray CT. The GDE morphology was characterized for its spatial porosity, tortuosity, pore-size, and solid-size distributions. At last, we discuss the water retention curves and scale-bridging between the findings from nano- and micro X-ray CT.

## 2. Materials

### 2.1. Fe-MSG catalyst synthesis

PGM-free materials were synthesized by a UNM-developed Sacrificial Support Method (SSM). A mixture of three nitrogen-rich organic precursors with mass ratio of 1:1:1, 2-Methylimidazole (MIMZ), Streptomycin (STR), and Gluceryl (GLU) in water, was deposited on the surface of two silica mixtures (1:1 by weight): OX-50 (a surface area ~50 m<sup>2</sup> g<sup>−1</sup>) and in-house synthesized monodispersed silica (a surface area ~5 m<sup>2</sup> g<sup>−1</sup>, particle size ~100 nm). The suspension of silica and organic precursors was mixed together by stirring followed by the addition of Fe(NO<sub>3</sub>)<sub>3</sub>·9H<sub>2</sub>O. The mass ratio between iron nitrate and organics was selected as 1:8. The hotplate temperature was increased to 35 °C and water was allowed to evaporate. The dry composite mixture was ground with mortar and pestle. The fine powder was heat treated in a nitrogen atmosphere (flow rate of 100 ccm) at T = 945 °C for 60 min. Silica was removed by means of 25 wt% HF and the duration of leaching was 25 h. The catalyst was washed by DI water, until neutral pH, and dried at T = 85 °C for ~12 h. The obtained powder was additionally heat treated in an NH<sub>3</sub> atmosphere (flow rate of 100 ccm) at T = 975 °C for 45 min.

## 3. Methods

### 3.1. MEA fabrication and tests

Inks for the MEA were prepared by mixing 75 mg of the catalyst with 1.2 g of 5 wt% Nafion solution and 3.5 ml of IPA (the nominal amount of solid Nafion was 45 wt%). The mixture was sonicated in an ultrasound bath for 2 h. A hand spraying technique was used to deposit 4 mg cm<sup>−2</sup> of catalyst onto the surface of 5 cm<sup>2</sup> of SGL 29BC carbon paper. The MEA was assembled by hot pressing the anode (Pt/C JM 0.5 mg cm<sup>−2</sup>), membrane (Nafion N211), and hand-sprayed cathode at T = 135 °C, t = 3 min, and a pressure of 1000 lbs.

Test conditions were selected to be H<sub>2</sub>/Air, T<sub>cell</sub> = 80 °C, 100%RH, 250 ccm flow rate for the anode, 200 ccm flow rate for cathode, and a backpressure of 20 psig.

### 3.2. SEM, TEM and XPS characterization

The morphologies of the synthesized material were determined by scanning electron microscopy (SEM, Hitachi S-5200 Nano SEM with an accelerating voltage of 10 keV) and transmission electron microscopy (TEM, JEOL 2010 instrument with an accelerating voltage of 200 keV). XPS spectra were acquired on a Kratos Axis Ultra DLD X-ray photoelectron spectrometer using a Al Kα source monochromatic operating at 150 W with no charge compensation. The base pressure was about

$2 \times 10^{-10}$  Torr, and the operating pressure was around  $2 \times 10^{-9}$  Torr. Survey and high-resolution spectra were acquired at pass energies of 80 eV and 20 eV respectively. The acquisition time for survey spectra was 2 min, for C 1s and O 1s spectra – 3 min, for N 1s – 30 min, and for Fe 2p – 40 min. Data analysis and quantification were performed using CasaXPS software. A linear background subtraction was used for the quantification of C 1s, O 1s, and N 1s spectra, while a Shirley background was applied to Fe 2p spectra. Sensitivity factors provided by the manufacturer were utilized. A 70% Gaussian/30% Lorentzian line shape was utilized in the curve-fit of N 1s.

### 3.3. Experimental details on synchrotron X-ray computed tomography

Micro X-ray CT was performed at Beamline 2-BM at Advanced Photon Source (APS) at Argonne National Laboratory (ANL). A double-multilayer monochromator was used to select 24 keV X-rays, and detection was with a LuAG scintillator and 5x lenses with a sCMOS PCO.Edge camera-giving a  $1.33 \mu\text{m}$  pixel dimension and a  $3.3 \text{ mm}$  horizontal FOV. For each scan, a 100 ms exposure time was used with 1025 acquired projections over a  $180^\circ$  rotation range. The resulting acquisition time is about 2 min. A  $3.2 \text{ mm}$  diameter circular sample was cut and pressed against the sample stage for imaging, held to the stage with an X-ray transparent membrane.

Nano X-ray CT images were acquired at Beamline 32-ID at APS at ANL. Energy was set at 8 keV with 1 s exposure time per projection. A Fresnel zone plate (FZP) with a 60 nm outermost zone width was used. 1800 back projections were acquired during the scan, what resulted in a total scan time of 36 min. An approximately  $80 \mu\text{m}$  sample was cut with a micromanipulator to fit into the FOV of  $80 \mu\text{m}$  and mounted onto a flat pin (which was then mounted onto the stage).

### 3.4. Image analysis

Phase retrieval and tomographic reconstructions (including stripe reduction filtering from sonograms with parameters of ‘ringSigma = 3’, ‘ringLevel = 8’, and ‘ringWavelet = db5’) were performed using TomoPy (open-source software developed at ANL) with the Gridrec algorithm [34] for micro-CT and the ASTRA toolbox for nano-CT [45,46]. For micro-CT image processing, a Butterworth filter was applied with parameters of 0.2 and 2. The optimal ‘rat’ value was found to be  $1 \times 10^{-4}$ , where ‘rat’ is defined as the ratio between beta and delta, the imaginary part and real part decrements in the refractive index of the sample material. Image segmentation and analysis were carried out with Fiji/ImageJ and Avizo Fire 8.1. Two phases were identified during segmentation, solid (GDL fiber, MPL, and catalyst layer (CL)) and void space, and were separated by thresholds determined both manually and with the Otsu algorithm [33]. Because an optimal ‘rat’ value was selected during phase-retrieval, the two phases showed clear distinction on the grey-scale histogram with two well-defined peaks identifying void and solid, thus no further filtering or advanced segmentation was necessary. For micro-CT data, the images were cropped to  $2 \text{ mm} \times 2 \text{ mm}$  in the in-plane direction, where the thickness varied depending on whether GDL, MPL, and CL were considered or the region of interest was limited to the CL only. For nano-CT data the image was cropped to  $18 \times 23 \mu\text{m}$  in the in-plane direction.

### 3.5. Morphological properties

Porosity was computed with Fiji/ImageJ using the binary histogram for the segmented images. The spatial distribution of porosity for the through-plane direction was computed with an in-house written macro for ImageJ. Solid-size distributions were extracted with the “Local Thickness” Fiji/ImageJ plugin. Local thickness is defined as the diameter of the largest sphere that fits inside the object and contains the point,  $\vec{p}$ , where more details can be found in [32]:

$$t(\vec{p}) = 2 \max(\{r | \vec{p} \in sph(\vec{x}, y) \subseteq \Omega, \vec{x} \in \Omega\}) \quad (1)$$

Three-dimensional volume rendering of the sample was performed with Avizo Fire 8.1.

### 3.6. Morphology-dependent transport properties

For tortuosity calculations, direct volumetric meshing of the domains was performed. For meshing, ImageJ was used to generate STL meshes with no binning. Each image-stack was padded with three blank slices on the top and bottom to have a uniform boundary condition. STL files were imported into GMSH v. 2.13.1 [36], where solid-space was meshed using 3D volumetric meshing and meshing was improved with 3D Netgen optimization. The solid-space mesh was saved as a NASTRAN file with the “.bdf” resolution and imported into Comsol Multiphysics 5.1 (COMSOL, Inc., Burlington, MA) as a mesh and physical domain.

For geometric tortuosity calculations, conservation of mass is used:

$$\nabla \cdot (K \nabla c) = 0 \quad (2)$$

where K is the transport coefficient set to 1 here; c is the species concentration.

Tortuosity here is defined as the ratio of the actual path length,  $L_e$ , to the Euclidean distance, L, squared:  $\tau = (L_e/L)^2$ . To quantify the transport-dependent morphological properties, tortuosity is calculated,

$$\tau = \frac{\epsilon}{K_{eff}/K} \quad (3)$$

where  $\epsilon$  is the porosity; K is the intrinsic transport coefficient, set to 1 in these simulations; and  $K_{eff}$  is the effective transport coefficient determined by,

$$K_{eff}/K = \frac{N}{A} \frac{L}{\Delta c} \quad (4)$$

where N is the superficial flux, A is the in-plane CL area, L is the domain thickness, and  $\Delta c$  is the concentration difference between the inlet and outlet (assumed to be  $\Delta c = 1$  for the simulations). To calculate the tortuosity, we solve a finite-element simulation through the CL using boundary conditions of  $c = 1$  and  $c = 0$  for the CL through-thickness boundaries respectively. In this study, tortuosity was computed for the solid portion of the CL. Similar framework can be used for void space but Knudsen diffusion has to be accounted for in smaller pores of the CL, as shown previously [37]. A no-flux condition is used for the other boundaries. Domain element statistics for the CL sample from micro-CT of size  $0.9 \times 0.9 \text{ mm}$  and thickness  $170 \mu\text{m}$  were: 1,575,501 number of total (tetrahedral) elements, minimum element quality of  $1.287 \times 10^{-10}$ , average element quality 0.46. For the nano-CT sample with domain of size  $9.8 \times 11 \mu\text{m}$  and thickness  $11 \mu\text{m}$ : 356,446 number of total elements, average element quality of 0.385.

## 4. Results

### 4.1. Materials characterization

Previously, we formulated the requirements of the organic precursors to be implemented into the sacrificial support method (SSM) [5,6]. In general, a substantial amount of carbon atoms is needed to create an open-framed structure while nitrogen is needed for the creation of active sites. In many cases, it is impossible to find such a combination in one single molecule, thus, in the present work, the mixture of organic precursors was used. The concept of blending the precursors relies on the fact that different chemical compounds may contribute different reactive moieties in the high-temperature (pyrolytic) synthesis process. Methylimidazole is rich with nitrogen but depleted in carbon; Streptomycin is a source of carbon with nitrogen in the structure; and glucoril has a higher decomposition temperature

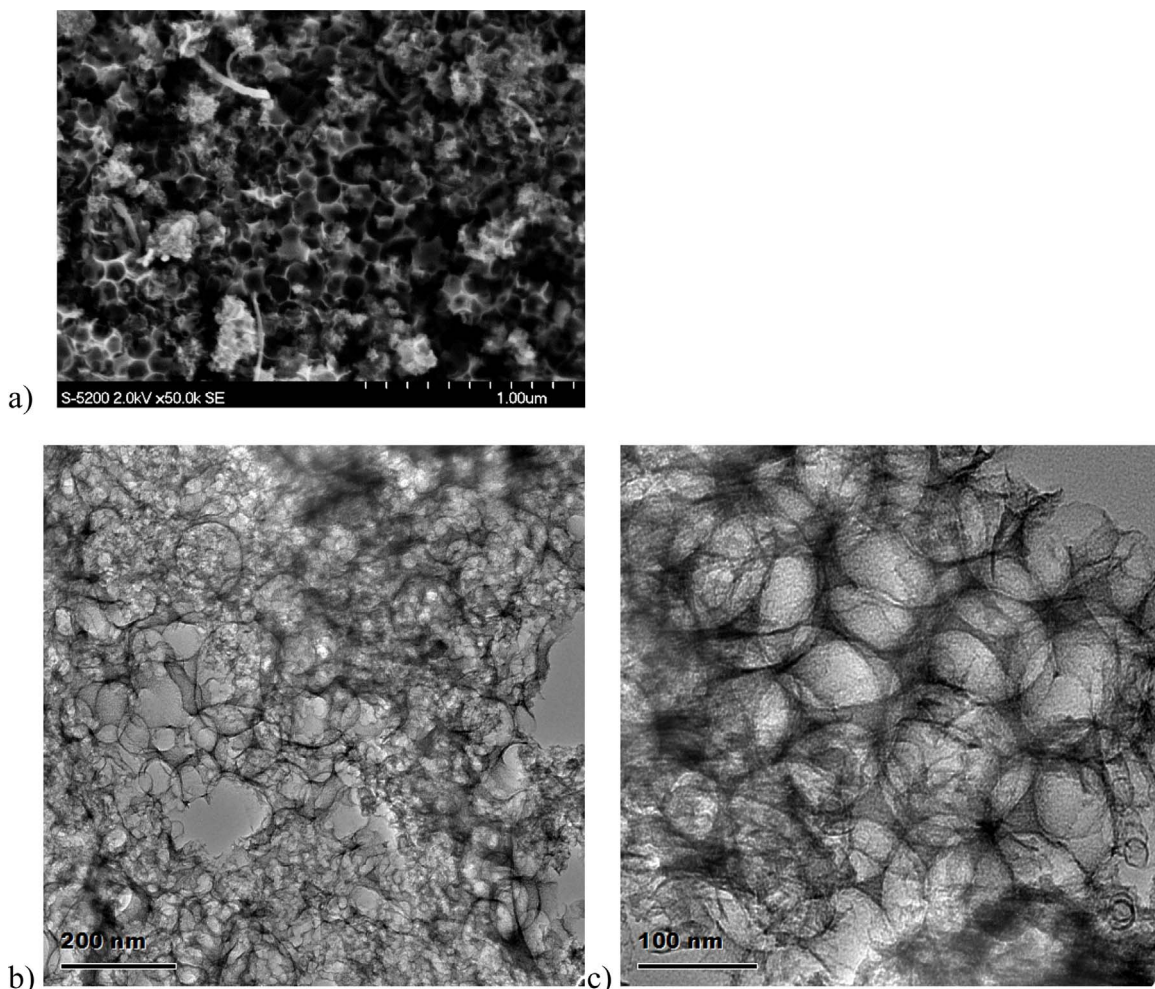


**Fig. 1.** SEM and TEM images of Fe-MSG catalyst prepared by Sacrificial Support Method.

resulting in the formation of additional nitrogen-contained active centers before volatilization of nitrogen groups.

It was shown previously that SSM allows full control over the morphology of different types of catalysts [4,5]. In general, the materials possess several modes of pores with pore size distribution in the range of 7 nm and larger than 50 nm [7,8]. Taking into account that the size of Nafion micelles is in the range of 30 nm [38], the majority of small pores cannot be in direct contact with Nafion and can only participating in the ORR when in contact with water. In the present work, SSM was modified in order to increase the amount of larger pores by the introduction of additional silica sacrificial support. Monodispersed silica, with particle size of ~100 nm, was used as an additive to low surface area commercial fumed silica. As shown by Fig. 1a, the morphology observed by SEM confirmed the success of using this approach.

The material has a high density of large pores which are an inverse replica of removed silica particles. Analysis of Fe-MSG by TEM revealed that the fine morphology of catalysts also consists of a highly porous 3D structure, as observed in UNM previous works (Fig. 1b) [9], while larger semi-spherical pores, formed by leaching of larger silica particles, are clearly seen too (Fig. 1c). The size of larger pores is exactly on the level of 100 nm which is giving, to SSM, an additional level of morphology control of macro-pores. The results of SEM and TEM confirm each other being complementary.

The catalyst powder was analyzed by XPS. Typical, for Fe-N-C catalysts made by SSM, amounts of nitrogen and iron were detected, i.e. 3.8 and 0.1 at.%, respectively. Fig. 2a shows high resolution N 1s spectrum along with individual peaks used to fit the experimental curve.

Major species that are present are pyridinic N at 398 eV, hydrogenated (such as pyrrolic and hydrogenated pyridine) N at 400.7 eV, and nitrogen coordinated to metal at 399.5 eV. At higher binding energies, peaks due to NO<sub>x</sub> (between 404 and 408 eV), graphitic N (between 402 and 404 eV), and cationic N (403 eV) are also identified. Fig. 2b shows high resolution carbon spectrum. A major component is the graphitic carbon of the graphene network. At the same time, a significant amount of defects in graphene are manifested in peaks due to various C=O species, such as C=O (286.5 eV), C=O (288 eV), COOH (289.5 eV), and C=N<sub>x</sub> defects (286.2 eV).

#### 4.2. Electrochemical performance

Polarization curve was collected for this study, where MEA was fabricated by catalyst coated substrate (CCS) method. The results from the rotating ring disk experiment are shown in Supplementary Info. Previously, many parameters for MEA fabrication with PGM-free catalysts were optimized by our group. [14,39] We selected ionomer loading, depositing method, hot pressing conditions, and catalyst loading based on previous experience with catalyst layer design obtained by our group. [14] Therefore, the MEA in this study is fairly representative of a class of MEA prepared previously. The results of the polarization curve recorded in an H<sub>2</sub>/Air fuel cell configuration under Department of Energy protocol conditions are shown in Fig. 3. The peak current density observed on the level of 250 mW cm<sup>-2</sup> is similar to our previous state-of-the-art performances [40].

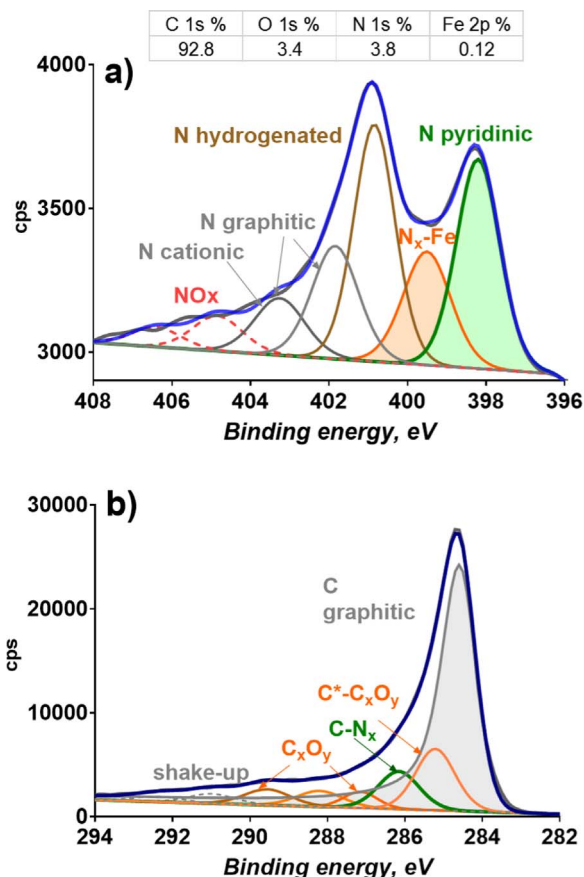


Fig. 2. High resolution spectra of Fe-MSG sample a) N 1s and b) C 1s.

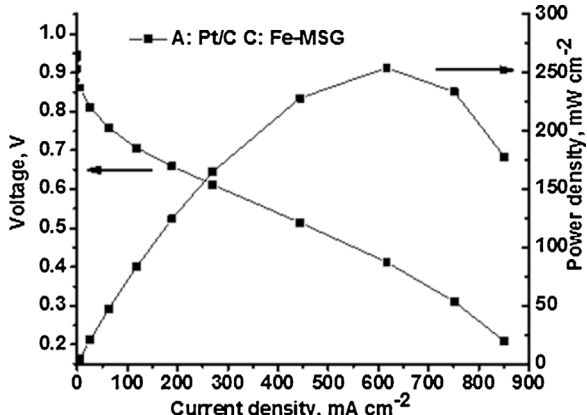


Fig. 3. MEA performance of Fe-MSG. Conditions: T<sub>cell</sub> = 80 °C, RH = 100%, H<sub>2</sub> back-pressure = 30 psig, Air backpressure = 30 psig. Anode: Pt/C, 0.2 mg cm<sup>-2</sup>(Pt), cathode: Fe-MSG, 4 mg cm<sup>-2</sup>.

#### 4.3. Morphology discussion

To understand electrode morphology, we perform a detailed analysis of the electrode micro- and nano- structure using both micro and nano X-ray CT. An MEA prepared from the same batch of ink was used. From the cross-section, grey-scale, and segmented tomographs shown by Fig. 4a, a dense layer of catalyst particles is formed at the interface with the MPL. Further away from the MPL, fewer catalyst aggregates form and large macropores are observed. We have also imaged MEAs with the other meso-structures and PGM-free chemistries (see Supplementary Info) prepared with the fabrication method described in the Experimental section, and we observed similar CL structures for thick

electrodes, indicating that the fabrication method is a controlling factor for morphology in the through-thickness direction. Furthermore, compressing the MEA between the GDLs and graphite plates did not change the CL structure significantly (see Supplementary Info), indicating that most of the stress is absorbed by the fibers in the GDLs.

From the in-plane view of the tomographs at different thickness locations, shown by Fig. 4b and c, the morphology of the CL changes significantly depending on the through-thickness location. 50 µm into the CL, as shown in Fig. 4b, the layer is composed of small (maximum diameter of 97.5 µm) but dense aggregates (macropore porosity is 0.4). Further away from the MPL, at the location of 90 µm into the thickness as shown in Fig. 4c, a lower density of aggregates is observed with a larger maximum diameter of 105 µm. This trend of lower density but larger size aggregates is preserved, as 104 µm into the CL thickness the aggregate's maximum radius is 113 µm, but they are distributed sparsely occupying only 10% of cross-section area (macropore porosity is 0.9). The catalyst layer thickness was measured at 15 locations via imaging, and the average value of 115 µm was obtained with a standard deviation of 33 µm.

Three-dimensional volume rendering shows large CL aggregates formed on the top of the MPL as shown in Fig. 5, where the fibrous domain is the GDL and top of the sample is the top of the CL. The image also shows cross-section grey-scale images to ensure that the volume-rendering was representative of the actual CL morphology. No significant artifacts were observed. Furthermore, volume rendering of a 20 µm cube of the CL shows uniform nano-structure within these larger aggregates.

#### 4.4. Porosity and solid-size distribution

To quantify the morphological features of the CL discussed in the previous section, here we use two metrics: porosity and solid-size distribution (SSD). In this study we assume aggregates (obtained with micro-CT) to be solid (porosity is 0). Thus the reported porosity is that of larger macropores. To quantify aggregate sizes we use the Local Thickness algorithm (inscribed spheres fitting into the domains) as described in the Methods section, where power-density function (PDF) represents SSD:

$$PDF(r) = \sum_{k=1,2} f_{r,k} \left\{ \frac{1}{r\sigma_k \sqrt{2\pi}} \exp \left[ -\frac{(\ln r - \ln r_{0,k})^2}{2\sigma_k^2} \right] \right\} \quad (5)$$

where  $PDF(r)$  is the normalized volume of solid aggregates having radius  $r$ ;  $f_{r,k}$  is the fraction of volume that makes up the distribution  $k$ , here taken to be 1, as it is unimodal distribution; and  $r_{0,k}$  and  $\sigma_k$  are the characteristic radius and spread of distribution  $k$  respectively.

The macroporous porosity of the sample is a function of thickness and exhibits a linear behaviour as Fig. 6a shows. At the interface with the MPL (location 0 thickness), the porosity is low, 0.38, which is due to a dense layer of CL aggregates near the MPL as confirmed by the cross-section tomographs shown by Fig. 4b. Due to solvent evaporation and drying far from the MPL, the porosity increases until it reaches values close to 1 at a location of 150 µm. The porosity is a strong function of the fabrication method, and it can be tailored accordingly. Large porosity is observed at the opposite end of the CL (towards the membrane), where fewer aggregates are present. This can result in layer delamination and degradation. From the nano-CT data, the porosity of the electrode on the nano-scale was uniform at 0.52. A representative elementary volume (REV) study was performed, and, for the CL with full thickness, the in-plane size has to be 400 µm or larger, as Supplementary Info, Fig. S2 shows. The FOV for nano-CT is smaller than that and hence it cannot capture the full FOV within a single scan.

The PDF or SSD for the aggregates is shown in Fig. 6b, where a unimodal log-normal distribution from the X-ray CT data is fit with the PDF fit as described by Eq. [5]. The average pore radius,  $r_{mean} = 12.2$  µm, was determined from the PDF as,

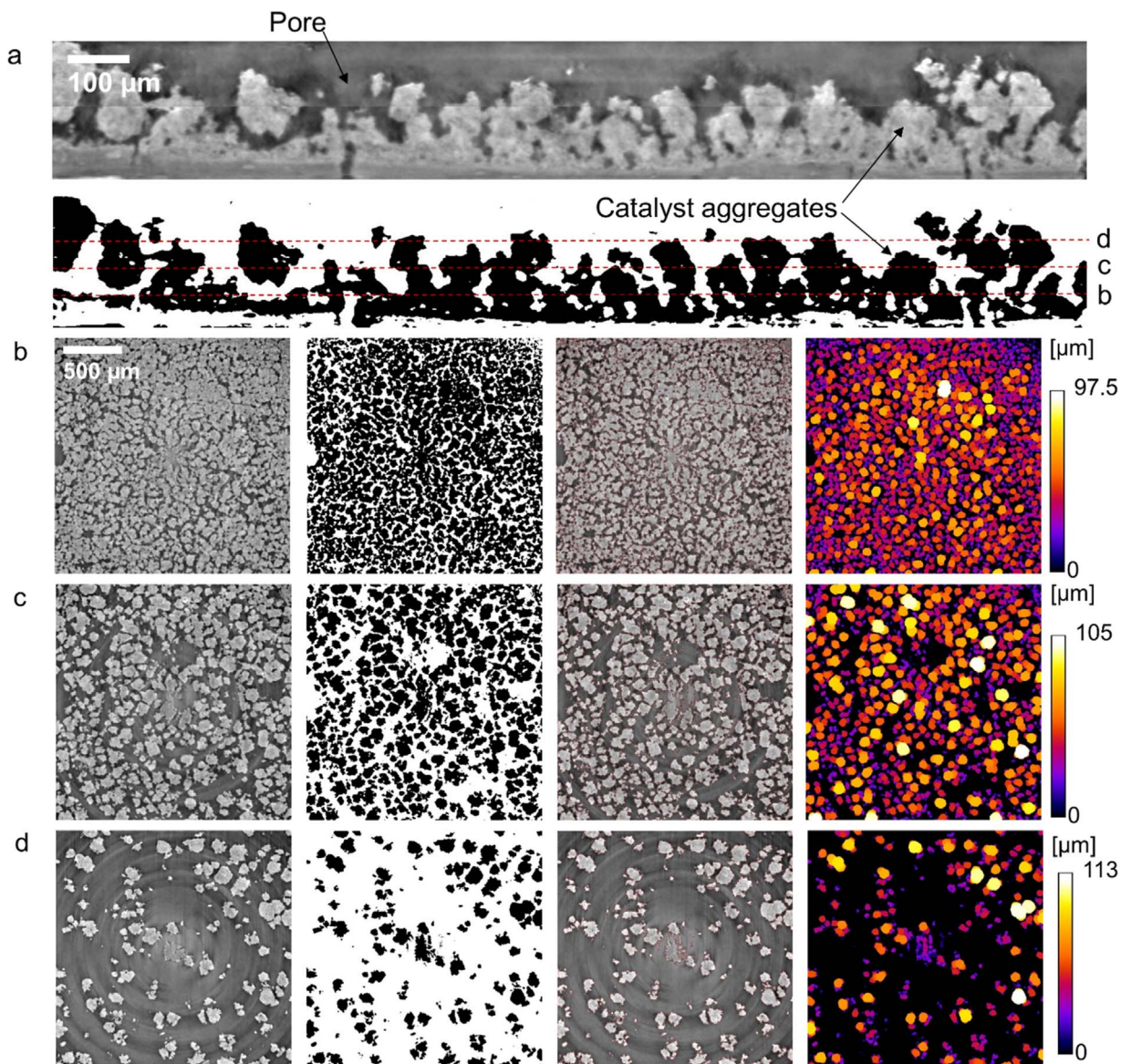


**Fig. 4.** a) Cross-section tomograph of CL, where the segmented image is compared to grey-scale. The selected cross-sections for b–d) are shown by dashed lines. In-plane views of locations b) 50 μm, c) 90 μm and d) 104 μm from MPL. Each row features grey-scale image, segmented, overlay of grey-scale and outline of segmented, and solid-size distributions with diameters shown by color-scheme on the right.

$r_{mean} = \int_0^{r_{max}} r \times PDF(r) dr$ , where the integration was taken over all existing radii. To put it in the perspective of the CL morphology, the CL thickness was 115 μm, and, if we were to represent the thickness with the spheres of mean CL radius, we would be able to fit about 5 spherical aggregates through the thickness of the CL. These large aggregates are clearly observed by Fig. 5 and also by volume-rendered Fig. 6. These large aggregates have meso-porosity described by Fig. 1, that is on the order of 100 nm or 0.1 μm, formed with monodispersed silica sacrificial substrate. From nano-CT data, a unimodal log-normal distribution was observed for the SSD with a mean radius of distribution of 0.16 μm as shown by Fig. 6c.

#### 4.5. Tortuosity

To quantify non-homogeneity of the CL morphology in the through-plane direction, we computed local tortuosity values for the CL, as shown by Fig. 7a. Tortuosity values for a solid portion of the domain is relevant as the solid portion, representing CL aggregates, is where

electron and proton transport takes place, thus this geometric property of the CL directly impacts ionic and electron conductivity. The CL sample of 0.9 × 0.9 mm and 172 μm thickness was considered. The tortuosity value for the first 52 μm next to the MPL was evaluated, and a low value of 1.8 was observed. From the concentration and streamline profiles shown by Fig. 7b, the flow is very uniform with multiple inlet and outlet locations. This is due to the large density of smaller CL aggregates present in this layer. For the layer of thickness 94 μm, the tortuosity value was also relatively low of 2. Once again, the flow profiles shown by Fig. 7c are very uniform with no observed disconnected regions between the top and the bottom portion of the CL. A large increase in tortuosity is observed for the layer of 134 μm thickness, the value of tortuosity almost doubled compared to the 52 μm volume. Fig. 7d shows dead-ended domains of aggregates that do not completely connect the top and bottom sides of the CL, that results in distorted streamlines as electron and proton transport will need to be redirected to avoid these dead-ended locations. At last, for the full-thickness domain, a large tortuosity value of 5.4 was observed. The flow profile shown by Fig. 7e shows only several entry locations at the top of the CL, which is the location that will be in contact with the membrane.

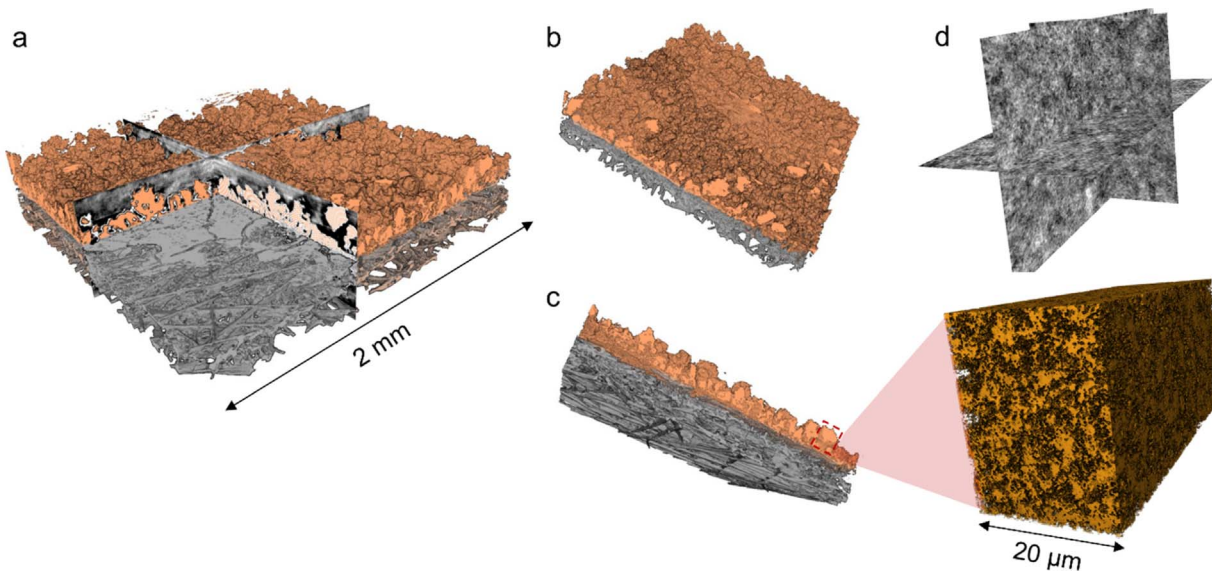


**Fig. 5.** Three dimensional volume-rendering of the CL, MPL and GDL, where GDL fibers are on the bottom and CL is on the top. a–c) Views from various perspectives. d) Grey-scale (top) and volume-rendered CL from nano-CT imaging.

High tortuosity values indicate poor solid-phase connectivity on the micro-scale. From nano-scale, tortuosity was computed for a CL portion of a width of 10  $\mu\text{m}$  as shown by Fig. 7f, where a relatively low tortuosity value of 2 was observed. Hence, the larger resistance to electron and proton transport in these thick PGM-electrodes is due to large tortuosity values for aggregates and not to smaller catalyst layer structures observed with nano-CT.

#### 4.6. Water retention curves

From the Young-Laplace equation, capillary pressure is defined as  $P_c = 2\gamma/r$ , where  $\gamma$  is surface tension, assumed to be a constant value of 0.625 N m; and  $r$  is the pore radius. In this analysis we assume that the CL is an ideally wetting porous medium. Because the electrode structure is highly non-uniform in the through-thickness direction, its water retention will also be non-uniform. We divide the CL into four through-thickness quarters ( $Q_1$  to  $Q_4$ ), as shown by Fig. 8c, and fit log-normal distributions to the PSDs shown by Fig. 8b. The mean radius,  $r_c$ , and the width of distribution,  $\sigma_c$ , for all four quarters, the full width, and also for nano-CT data are tabulated in Fig. 8d. From log-normal PSD, the saturation can be calculated as [41,42]:

$$s = \frac{1}{2} \left[ \left( 1 + \operatorname{erf} \left( \frac{\ln(r/r_c)}{\sqrt{2}\sigma_c} \right) \right) \right] \quad (6)$$

Water-retention curves, which are capillary pressure vs. saturation curves are plotted in Fig. 8a. The mesopores and micropores are filled at

high capillary pressure due to their small mean radii. The water retention curve for the nano-CT data is also in good agreement with the previous study done by Komini Babu et al. [37]. The macropores start filling at  $10^5$ – $10^6$  Pa depending on location within the CL. At the interface with the membrane ( $Q_4$ ) the macropores are the largest (Fig. 8b) and hence it takes the least pressure to invade them. Whereas, for the smaller pores at the base of the CL (interface with the MPL), the capillary pressure is relatively flat, indicative of a narrow PSD in that quarter. The water retention curve for the full thickness is shown as well, which has a steep slope due to the large width of the PSD (1.15  $\mu\text{m}$ ). For the modeling studies and accurate representation of the CL morphology and water transport, it is essential to bridge the scales between the meso- and macroscales; however, it is also critical to represent the CL as a composite domain, whether it is a pore-network or continuum model. Furthermore, nano-CT imaging is not sufficient to predict water transport processes in operating PEMFC and limiting current operation conditions. For the PGM-free electrodes, it is critical to bridge the findings from nano-CT and micro-CT on the meso- and macroscales. CL macrostructure obtained with micro-CT will determine interfacial water pooling that will primarily dictate water transport on the macroscale. Knowledge of local surface wettability is critical to properly describe water transport on meso- and macro-scales, as saturation depends on local surface tension [43,44].

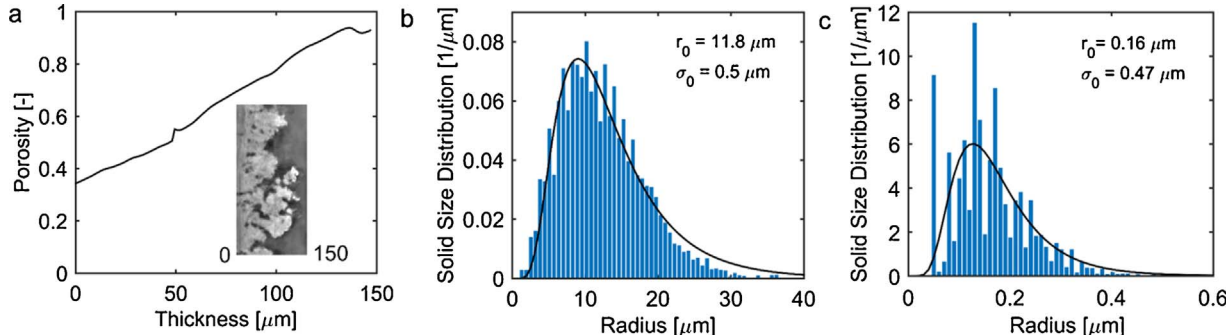


**Fig. 6.** a) Through-thickness porosity of the catalyst layer and b) micro-CT solid aggregates size distribution, where line shows a fit to a unimodal log-normal distribution, c) SSD for mesoscale obtained with nano-CT.

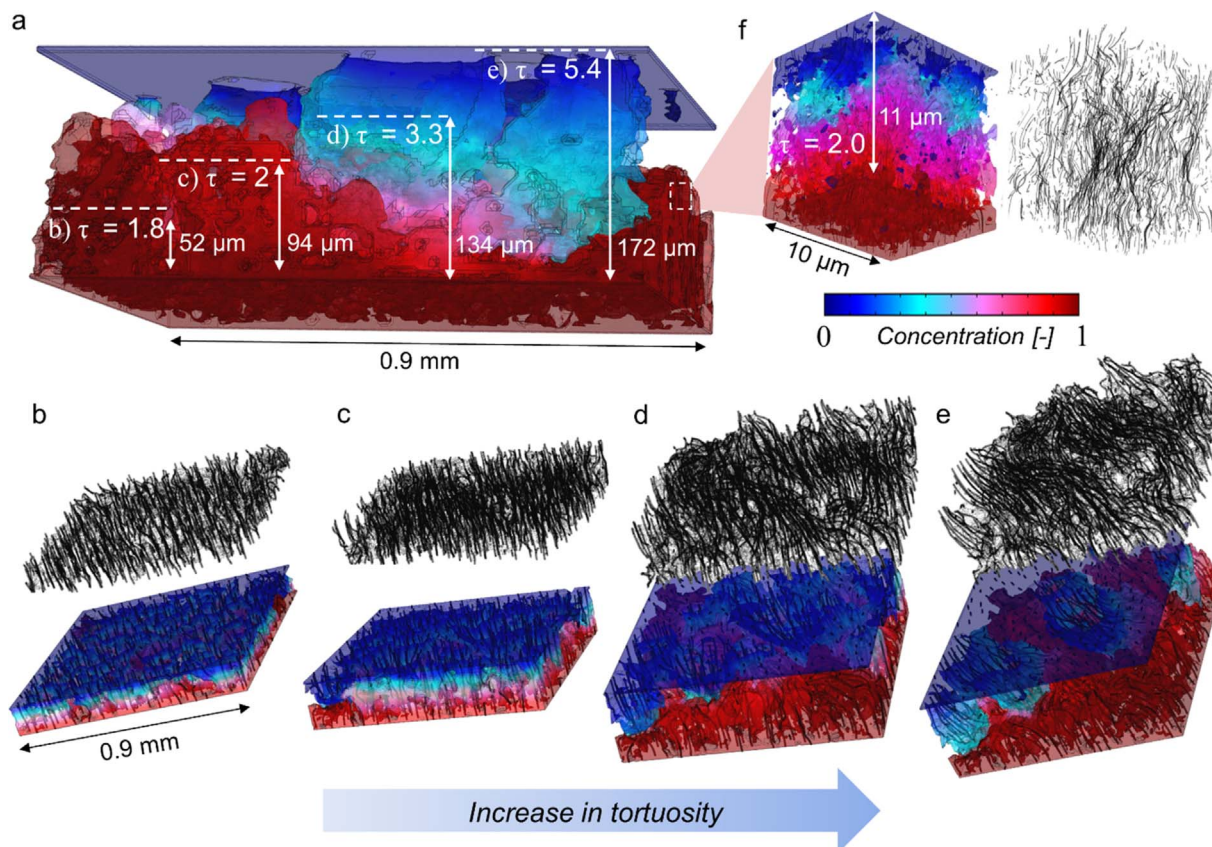


**Fig. 7.** Study of tortuosity as a function of sample thickness with micro-CT starting from the MPL interface, where a) shows full sample thickness and each sub-division. b–e) Samples of varied thicknesses. f) Mesoscale tortuosity obtained with nano-CT.

## 5. Conclusion

A novel PGM-free Fe-N-C catalyst was synthesized based on nitrogen-rich organic precursors and two types of silica sacrificial substrate. The electrocatalyst has shown meso-porosity on the order of the larger silica substrate of  $\sim 100$  nm and showed chemical and electrochemical performance comparable to the state-of-the-art catalysts developed within the group [10,14]. The three-dimensional micro X-ray

computed tomography (CT) revealed the through-thickness inhomogeneous morphology of the fabricated gas-diffusion electrode (GDE) with smaller and denser catalyst aggregates at the MPL and larger aggregates with larger voids in-between at the opposite end (near the membrane). The formed electrode structure exhibited a linear through-thickness porosity profile with an average aggregate of  $12.2 \mu\text{m}$ , a representative volume of  $0.4 \mu\text{m}$ , and a high tortuosity of 5.4. On the nano-scale, the morphology was uniform with an average

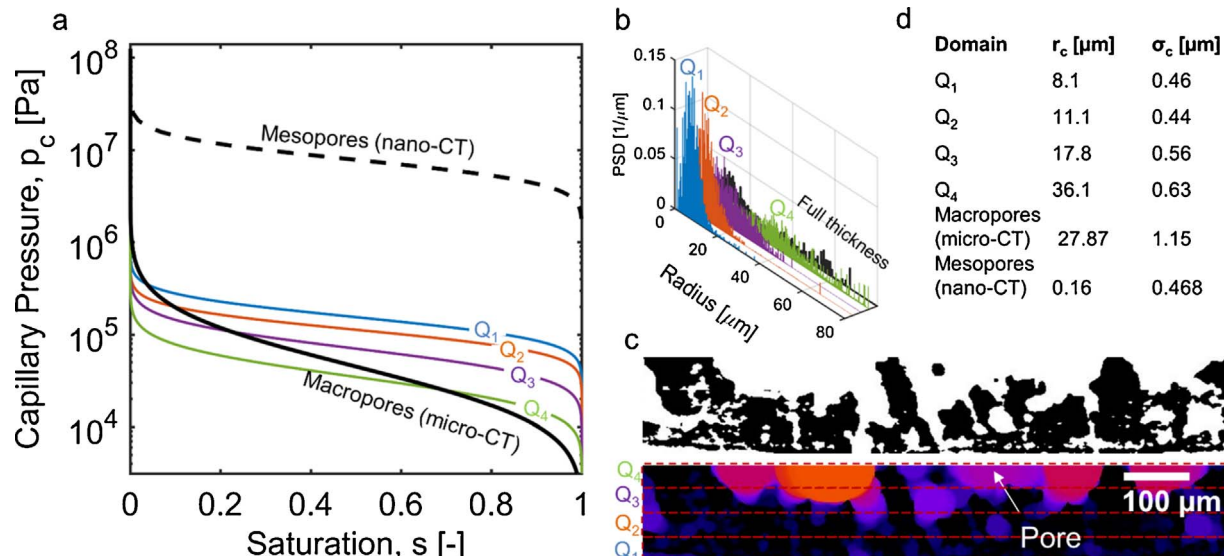


**Fig. 8.** a) Water retention curve for larger macropores and mesopores, b) PSD for four through-thickness quarters and full thickness of the PGM-free electrodes depicted in c), and parameters for water-retention curves are shown by d).

particle diameter of 0.16 µm and a porosity of 0.52. It was observed that the first half-thickness of the CL was more uniform with a low tortuosity of 2, which is also the tortuosity obtained with nano-CT imaging of mesoscale. However, the portion of the CL away from the substrate was strongly inhomogeneous with large voids resulting in an overall tortuosity of 5.4. Water retention curves showed significant spatial dependence on the macroscale, with relatively low capillary pressures to invade these pores. While the mesoporous structure obtained with nano-CT describes the morphology within larger aggregates well, micro-CT resolution is essential to describe the full thickness of the CL, which, for PGM-free materials, ranges in the order of 100 µm. Most of the spatial inhomogeneities are found on the macroscale.

Further studies are needed to understand the CL morphology when ink is directly deposited onto the membrane. With this method larger voids will form at the interface with the MPL, resulting in advantages and disadvantages to be explored in terms of transport processes and water management. Furthermore, a combined coating of ink (and/or catalyst loading through-thickness variations) onto a membrane and MPL needs to be investigated, where the interfacial gap will be within the CL itself.

## Acknowledgements

We thank Dr. Dula Parkinson and Mr. Luis Barroso Luque from Advanced Light Source for help with installation and configuration of TomoPy codes. This research used resources of the Advanced Photon Source, a U.S. Department of Energy (DOE) Office of Science User Facility operated for the DOE Office of Science by Argonne National Laboratory under Contract No. DE-AC02-06CH11357.

## Appendix A. Supplementary data

Supplementary data associated with this article can be found, in the online version, at <http://dx.doi.org/10.1016/j.apcatb.2017.08.067>.

## References

- [1] T. Yoshida, K. Kojima, *Electrochim. Soc. Interface* 24 (2015) 45–49.
- [2] [https://hydrogendoedev.nrel.gov/pdfs/progress10/v\\_a\\_3\\_sinha.pdf](https://hydrogendoedev.nrel.gov/pdfs/progress10/v_a_3_sinha.pdf).
- [3] C. Delacote, A. Bonakdarpour, C.M. Johnston, P. Zelenay, A. Wieckowski, *Faraday Discuss.* 140 (2009) 269–281.
- [4] A.A. Serov, S.-Y. Cho, S. Han, M. Min, G. Chai, K.H. Nam, C. Kwak, *Electrochim. Commun.* 9 (2007) 2041–2044.
- [5] A.A. Serov, M. Min, G. Chai, S. Han, S. Kang, C. Kwak, *J. Power Sources* 175 (2008) 175–182.
- [6] A.A. Serov, C. Kwak, *Catal. Commun.* 10 (2009) 1551–1554.
- [7] A.A. Serov, T. Nedoseykina, O. Shvachko, C. Kwak, *J. Power Sources* 195 (2010) 175–180.
- [8] A. Garsuch, X. Michaud, K. Böhme, G. Wagner, J.R. Dahn, *J. Power Sources* 189 (2009) 1008–1011.
- [9] M. Shao, Q. Chang, J.-P. Dodelet, R. Chenitz, *Chem. Rev.* 116 (2016) 3594–3657.
- [10] A. Serov, K. Artyushkova, P. Atanassov, *Adv. Energy Mater.* 4 (2014) (1301735-n/a).
- [11] X. Ge, A. Sumboja, D. Wuu, T. An, B. Li, F.W.T. Goh, T.S.A. Hor, Y. Zong, Z. Liu, *ACS Catal.* 5 (2015) 4643–4667.
- [12] M.J. Workman, A. Serov, B. Halevi, P. Atanassov, K. Artyushkova, *Langmuir* 31 (2015) 4924–4933.
- [13] L. Dai, Y. Xue, L. Qu, H.-J. Choi, J.-B. Baek, *Chem. Rev.* 115 (2015) 4823–4892.
- [14] S. Stariba, K. Artyushkova, M.J. Workman, A. Serov, S. McKinney, B. Halevi, P. Atanassov, *J. Power Sour.* 326 (2016) 43–49.
- [15] C. Zhu, H. Li, S. Fu, D. Du, Y. Lin, *Chem. Soc. Rev.* 45 (2016) 517–531.
- [16] Y. Nie, L. Li, Z. Wei, *Chem. Soc. Rev.* 44 (2015) 2168–2201.
- [17] A. Serov, U. Tylus, K. Artyushkova, S. Mukerjee, P. Atanassov, *Appl. Catal. B: Environ.* 150–151 (2014) 179–186.
- [18] I.M. Mosa, S. Biswas, A.M. El-Sawy, V. Botu, C. Guild, W. Song, R. Ramprasad, J.F. Rusling, S.L. Suib, *J. Mater. Chem. A* 4 (2016) 620–631.
- [19] M.H. Robson, A. Serov, K. Artyushkova, P. Atanassov, *Electrochim. Acta* 90 (2013) 656–665.
- [20] R.J. Toh, Z. Sofer, M. Pumera, *ChemPhysChem* 16 (2015) 3527–3531.
- [21] R.P. Kingsborough, T.M. Swager, *Chem. Mater.* 12 (2000) 872–874.
- [22] J. Shui, C. Chen, L. Grabstanowicz, D. Zhao, D.-J. Liu, *Proc. Natl. Acad. Sci.* 112 (2015) 10629–10634.
- [23] Y.-C. Wang, Y.-J. Lai, L. Song, Z.-Y. Zhou, J.-G. Liu, Q. Wang, X.-D. Yang, C. Chen, W. Shi, Y.-P. Zheng, M. Rauf, S.-G. Sun, *Angew. Chem. Int. Ed.* 54 (2015) 9907–9910.
- [24] L. Yang, N. Larouche, R. Chenitz, G. Zhang, M. Lefèvre, J.-P. Dodelet, *Electrochim. Acta* 159 (2015) 184–197.
- [25] H.A. Gasteiger, S.S. Kocha, B. Sompalli, F.T. Wagner, *Appl. Catal. B-Environ.* 56 (2005) 9–35.
- [26] N.D. Leonard, K. Artyushkova, B. Halevi, A. Serov, P. Atanassov, S.C. Barton, J. *Electrochem. Soc.* 162 (2015) F1253–F1261.
- [27] T. Lopes, A. Kucernak, D. Malko, E.A. Ticianelli, *ChemElectroChem* 3 (2016) 1580–1590.
- [28] P. Zelenay, *ElectroCat Workshop*, Argonne National Laboratory, 2016.
- [29] S. Komini Babu, H.T. Chung, G. Wu, P. Zelenay, S. Litster, *ECS Trans.* 64 (2014) 281–292.
- [30] D. Spernjak, H.T. Chung, R. Mukundan, R.L. Borup, D.S. Hussey, D.L. Jacobson, G. Wu, P. Zelenay, *Meeting Abstracts*, MA2015–02 (2015) 1540.
- [31] M. Arif, D.S. Hussey, E.M. Baltic, D.L. Jacobson, *Phys. Procedia* 69 (2015) 210–217.
- [32] I.V. Zenyuk, D.Y. Parkinson, L.G. Connolly, A.Z. Weber, *J. Power Sources* 328 (2016) 364–376.
- [33] I.V. Zenyuk, D.Y. Parkinson, G. Hwang, A.Z. Weber, *Electrochim. Commun.* 53 (2015) 24–28.
- [34] D. Gürsoy, F. De Carlo, X. Xiao, C. Jacobsen, *Tomopy: a framework for the analysis of synchrotron tomographic data*, *J. Synchrotron. Radiat.* 21 (5) (2014) 1188–1193.
- [35] C. Geuzaine, J.-F. Remacle, *Int. J. Numer. Methods Eng.* 79 (2009) 1309–1331.
- [36] S. Komini Babu, H.T. Chung, P. Zelenay, S. Litster, *ACS Appl. Mater. Interfaces* 8 (48) (2016) 32764–32777.
- [37] H. Zhang, J. Pan, X. He, M. Pan, *J. Appl. Polym. Sci.* 107 (2008) 3306–3309.
- [38] S. Stariba, K. Artyushkova, A. Serov, P. Atanassov, *Int. J. Hydrogen Energy* 40 (2015) 14676–14682.
- [39] A. Serov, M.J. Workman, K. Artyushkova, P. Atanassov, G. McCool, S. McKinney, H. Romero, B. Halevi, T. Stephenson, *J. Power Sources* 327 (2016) 557–564.
- [40] I.V. Zenyuk, E.C. Kumbur, S. Litster, *J. Power Sources* 241 (2013) 379–387.
- [41] A.Z. Weber, R.L. Borup, R.M. Darling, P.K. Das, T.J. Dursch, W. Gu, D. Harvey, A. Kusoglu, S. Litster, M.M. Mench, R. Mukundan, J.P. Owejan, J.G. Pharoah, M. Secanell, I.V. Zenyuk, *J. Electrochim. Soc.* 161 (2014) F1254–F1299.
- [42] I.V. Zenyuk, P.K. Das, A.Z. Weber, *J. Electrochim. Soc.* 163 (2016) F691–F703.
- [43] P.K. Das, X. Li, Z. Xie, Z.-S. Liu, *Int. J. Energy Res.* 35 (2011) 1325–1339.
- [44] D. Pelt, D. Gürsoy, W.J. Palenstijn, J. Sijbers, F. De Carlo, K.J. Batenburg, *Integration of tomopy and the astra toolbox for advanced processing and reconstruction of tomographic synchrotron data*, *J. Synchrotron. Radiat.* 23 (3) (2016) 842–849.
- [45] V. De Andrade, A. Deriy, M.J. Wojcik, D. Gürsoy, D. Shu, K. Fezzaa, F. De Carlo, *Nanoscale 3D imaging at the Advanced Photon Source*, SPIE Newsroom (2016), <http://dx.doi.org/10.1117/2.1201604.006461>.
- [46] I.V. Zenyuk, A.Z. Weber, *ECS Trans.* 69 (2015) 1253–1265.

## Further reading

- [35] I.V. Zenyuk, A.Z. Weber, *ECS Trans.* 69 (2015) 1253–1265.